Structures of Tetrahydrobiopterin Binding-Site Mutants of Inducible Nitric Oxide Synthase Oxygenase Dimer and Implicated Roles of Trp457[†,‡]

Mika Aoyagi,[§] Andrew S. Arvai,[§] Sanjay Ghosh,[||,⊥] Dennis J. Stuehr,[||] John A. Tainer,[§] and Elizabeth D. Getzoff*[,§]

Department of Molecular Biology, The Skaggs Institute for Chemical Biology, The Scripps Research Institute, La Jolla, California 92037, and Department of Immunology, The Lerner Research Institute, Cleveland Clinic Foundation, Cleveland, Ohio 44195

Received June 8, 2001; Revised Manuscript Received August 22, 2001

ABSTRACT: To better understand potential roles of conserved Trp457 of the murine inducible nitric oxide synthase oxygenase domain ($iNOS_{ox}$; residues 1−498) in maintaining the structural integrity of the (6*R*)-5,6,7,8-tetrahydrobiopterin (H_4B) binding site located at the dimer interface and in supporting H_4B redox activity, we determined crystallographic structures of W457F and W457A mutant $iNOS_{ox}$ dimers (residues 66−498). In W457F $iNOS_{ox}$, all the important hydrogen-bonding and aromatic stacking interactions that constitute the H_4B binding site and that bridge the H_4B and heme sites are preserved. In contrast, the W457A mutation results in rearrangement of the Arg193 side chain, orienting its terminal guanidinium group almost perpendicular to the ring plane of H_4B. Although Trp457 is not required for dimerization, both Trp457 mutations led to the increased mobility of the N-terminal H_4B binding segment (Ser112−Met114), which might indicate reduced stability of the Trp457 mutant dimers. The Trp457 mutant structures show decreased π-stacking with bound pterin when the wild-type π-stacking Trp457 position is occupied with the smaller Phe457 in W457F or positive Arg193 in W457A. The reduced pterin π-stacking in these mutant structures, relative to that in the wild-type, implies stabilization of reduced H_4B and destabilization of the pterin radical, consequently slowing electron transfer to the heme ferrous−dioxy ($Fe^{II}O_2$) species during catalysis. These crystal structures therefore aid elucidation of the roles and importance of conserved Trp457 in maintaining the structural integrity of the H_4B binding site and of H_4B-bound dimers, and in influencing the rate of electron transfer between H_4B and heme in NOS catalysis.

Nitric oxide synthases (NOSs)[1] catalyze the five-electron oxidation of L-arginine (L-Arg) to produce L-citrulline and nitric oxide (NO), an important signaling molecule and cytotoxin in biological systems. The reaction proceeds via formation of an enzyme-bound stable intermediate, N^{ω}-hydroxy-L-arginine (NOHA) (*1, 2*). Three distinct NOS isoforms, inducible (iNOS), endothelial (eNOS), and neuronal (nNOS), have been identified in mammalian systems. All isoforms require dimerization for activity and share a similar basic domain architecture: (1) the N-terminal catalytic oxygenase domain (NOS_{ox}; amino acids 1−498 in murine iNOS) which binds Fe-protoporphyrin IX (heme), substrate L-Arg, and (6*R*)-5,6,7,8-tetrahydrobiopterin (H_4B); (2) the central linker region (amino acids 499−530 for murine iNOS) that binds calmodulin (CaM); and (3) the C-terminal electron-supplying reductase domain (NOS_{red}; amino acids 531−1144 in murine iNOS) with binding sites for flavin mononucleotide (FMN), flavin adenine dinucleotide (FAD), and NADPH (*3*−*6*). In the biologically active NOS homodimer, CaM binding to the central linker region mediates electron transfer from NOS_{red} of one subunit *in trans* to NOS_{ox} of the other subunit of the dimer (*7, 8*).

NOSs are the only enzymes known to contain both heme and H_4B. H_4B has combined structural and electronic roles in NOS catalysis which despite extensive study are still not fully understood. In iNOS, H_4B facilitates subunit interactions (*9*−*14*), decreases the susceptibility of Lys117 to proteolytic cleavage (*15*), and increases the affinity for L-Arg (*16*). Based on biochemical studies showing that H_4B analogues, such as 7,8-dihydrobiopterin (H_2B) and 4-amino-5,6,7,8-tetrahydrobiopterin (4-amino-H_4B), can mimic the aforementioned allosteric effects, but do not support iNOS catalysis (*16, 17*), an electronic role for H_4B was anticipated. Indeed, H_4B likely participates in redox chemistry during NOHA formation (*18*), and a pterin radical was detected during $iNOS_{ox}$ catalysis by electron paramagnetic resonance (EPR) experiments (*19, 20*). The redox roles of H_4B seem to justify the absolute requirement of H_4B for catalysis in all three isozymes, whereas the allosteric and structural effects of H_4B vary among isozymes.

[†] Supported by National Institutes of Health Grant HL58883 (E.D.G.).

[‡] PDB codes for the structures are reported within: W457F $iNOS_{ox}$ (IJWJ); W457A $iNOS_{ox}$ (IJWK).

* To whom correspondence should be addressed. Telephone: (858)-784-2878. Fax: (858)-784-2289. E-mail: edg@scripps.edu.

[§] The Scripps Research Institute.

[||] The Lerner Research Institute.

[⊥] Present address: Department of Biochemistry, University College of Sciences, Calcutta 700 019, India.

[1] Abbreviations: BOG, *N*-octyl-β-D-glucopyranoside; CaM, calmodulin; H_2B, 7,8-dihydrobiopterin; eNOS, endothelial nitric oxide synthase; EPR, electron paramagnetic resonance; 4-amino-H_4B, 4-amino-5,6,7,8-tetrahydrobiopterin; H_4B, (6*R*)-5,6,7,8-tetrahydrobiopterin; iNOS, inducible nitric oxide synthase; L-Arg, L-arginine; MES, 2-(*N*-morpholino)ethanesulfonic acid; NOHA, N^{ω}-hydroxy-L-arginine; nNOS, neuronal nitric oxide synthase; NO, nitric oxide; NOS, nitric oxide synthase; NOS_{ox}, nitric oxide synthase oxygenase domain; NOS_{red}, nitric oxide synthase reductase domain.

10.1021/bi011183k CCC: $20.00
Published on Web 09/29/2001

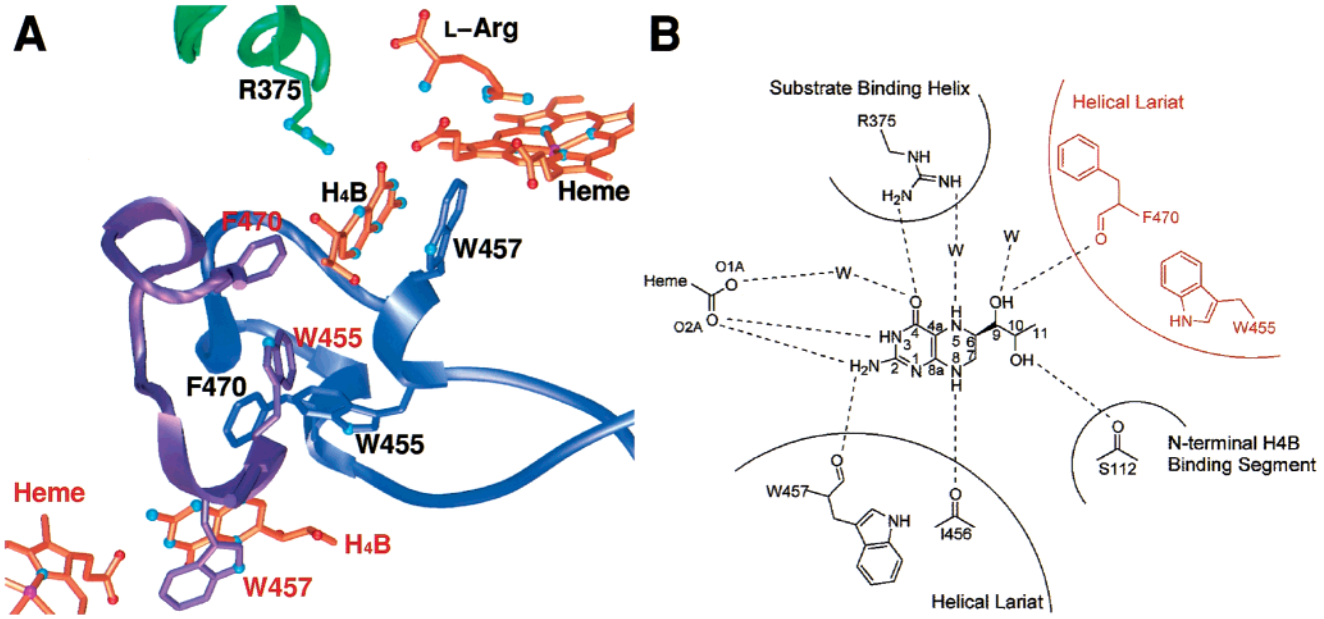

FIGURE 1: Structural coupling among H_4B binding, dimerization, and substrate binding. Residues and cofactors of the adjacent subunit are labeled in red (PDB code 1NOD). (A) Secondary structure elements linking H_4B binding, substrate binding, and dimerization. The substrate binding helix (green) provides the conserved Arg375 for H_4B binding, and helical lariats (blue, subunit A; purple, subunit B) contain aromatic residues interacting with H_4B bound on each subunit of the dimer. (B) A schematic diagram of key hydrogen-bonding (dashed lines) and π-stacking interactions in panel A. Protein residues provided by the helical lariat of the other subunit are indicated in red.

Crystal structures of dimeric $iNOS_{ox}$ indicate that the H_4B site (Figure 1) is formed by aromatic residues contributed by both subunits at the dimer interface, and is structurally and electronically coupled to the heme active site via a hydrogen bond network, which tunes the H_4B protonation and resonance states (*21*, *22*). Side chains of Trp455 and Phe470 on the helical lariat of one subunit stack against H_4B bound to another subunit of the dimer (Figure 1A). Although the location of H_4B with respect to the heme eliminates the possibility that the cofactor directly participates in hydroxylating the substrate L-Arg (*21*), H_4B forms hydrogen bonds from N3 directly and O4 indirectly through a water molecule to heme propionate A (Figure 1B), which also interacts with the α-amino group of L-Arg. H_4B O4 and N5 also form hydrogen bonds to Arg375, which is located on the substrate binding helix (Figure 1B). Trp457 forms π-stacking (Figure 1A) and hydrogen-bonding (Figure 1B) interactions with H_4B bound to the same subunit via its indole ring and backbone carbonyl, respectively. The indole ring is sandwiched between H_4B and the guanidinium group of Arg193, which is linked by hydrogen bonds through the Tyr485 hydroxyl to heme propionate B. These residues, which form critical interactions with H_4B, are highly conserved among different NOS isoforms (*21*, *23*−*25*).

The roles of Trp457, which forms extensive π-stacking interactions with H_4B, in dimer formation, H_4B and L-Arg binding, and catalysis have been investigated by site-directed mutagenesis studies. Although both W457F and W457A $iNOS_{ox}$ dimerize in the presence of H_4B and/or L-Arg, the mutations lead to reduced H_4B and L-Arg affinity, and slower NO synthesis (*26*). Sagami et al. also reported that W678L nNOS (equivalent to Trp457 in murine iNOS) dimerizes in the presence of L-Arg and H_4B, but exhibits a slow rate of heme reduction by NADPH and no NO formation (*27*). These biochemical analyses indicate that Trp457 may play important functional roles in H_4B-supported NO synthesis and, to a lesser extent, in H_4B-mediated dimer stabilization.

To address the structural biochemistry of Trp457 in NOS function, we present here the crystal structures of W457F and W457A $iNOS_{ox}$ refined to 2.6 and 2.3 Å resolution, respectively. Structural reorganization associated with each mutation is examined to assess potential roles of Trp457 in controlling the structural integrity of the H_4B binding site, H_4B-mediated dimer stability, and electron transfer during NO synthesis. In the accompanying paper, Wang et al. (*28*) report effects of these Trp457 mutations on heme transitions, pterin radical formation, and NOHA formation during a single turnover reaction of $iNOS_{ox}$. Together, our results help establish how the conserved Trp457 mediates H_4B-supported NOS activity.

EXPERIMENTAL PROCEDURES

Protein Preparation and Crystallization. Recombinant murine W457F and W457A $iNOS_{ox}$ Δ65 (residues 66−498) were overexpressed and purified from *Escherichia coli*, as described previously (*21*, *26*, *29*). Residues 66−498 of murine $iNOS_{ox}$ were previously shown to be sufficient to form a functional dimeric enzyme (*15*). Unless otherwise noted, all crystallization experiments were performed using the hanging drop technique at 4 °C in the presence of 4 mM H_4B and 10 mM AR-C95791AA, an N-substituted aminopyridine NOS inhibitor, supplied by AstraZeneca. AR-C95791AA, which like substrate L-Arg (*21*) stacks on the heme distal side and forms a bidentate salt bridge to Glu371, improves crystal stability and diffraction quality (details of AR-C95791AA interactions in the substrate binding site to be published elsewhere). A 1−2 μL aliquot of the purified mutant protein (20 mg/mL) in 40 mM *N*-(2-hydroxyethyl)-piperazine-*N*′-3-propanesulfonic acid (EPPS), pH 7.6, was mixed with an equal volume of reservoir solution containing

Table 1: Crystallographic Data Collection and Refinement Statistics for W457F and W457A $iNOS_{ox}$

structure	W457F	W457A
wavelength (Å)	1.0	1.08
cell dimensions (Å)	$a = b = 213.6$, $c = 116.9$	$a = b = 213.5$, $c = 116.2$
data resolution (Å)	50.0−2.6 (2.69−2.60)[a]	20.0−2.3 (2.38−2.30)
total observations	142979	490274
unique observations	46998	63261
completeness (%)	97.2 (87.0)	91.4 (59.7)
$\langle I/\sigma \rangle$[b]	15.1 (2.0)	31.6 (1.8)
R_{sym}[c]	0.07 (0.45)	0.04 (0.38)
R[d]	0.218	0.218
R_{free}[e]	0.257	0.244
no. of non-H atoms	7255	7351
no. of waters	335	461
⟨overall B⟩ (Å^2)	47.6	44.5
⟨main chain B⟩ (Å^2)	46.8	43.5
⟨side chain B⟩ (Å^2)	48.6	45.8
rms bond (Å)	0.0073	0.0065
rms angle (deg)	1.3	1.3

[a] Highest resolution shell for compiling statistics. [b] Average intensity signal-to-noise ratio. [c] $R_{sym} = \sum\sum_j |I_j - \langle I \rangle| / \sum\sum_j I_j$. [d] $R = \sum ||F_o| - |F_c|| / \sum |F_o|$, where F_o and F_c are the observed and calculated structure factors, respectively. [e] 5% of the reflections were set aside randomly for R_{free} calculation.

27−30% saturated ammonium sulfate, 50 mM 2-(*N*-morpholino)ethanesulfonic acid (MES), pH 5−6, 10−30 mM *N*-octyl-*β*-D-glucopyranoside (BOG), and 15−30 mM dithiothreitol. Crystals of both mutant proteins were isomorphous with those previously reported for wild-type $iNOS_{ox}$ Δ65, belonging to space group $P6_122$ with unit cell dimensions $a = b = \sim 214$ Å, $c = \sim 117$ Å, 2 molecules per asymmetric unit, and a solvent content of 70% (*21, 22, 30*).

Data Collection and Structure Determination. Table 1 summarizes statistics for diffraction data collection and crystallographic refinement. The data for W457F and W457A $iNOS_{ox}$ were collected from flash-cooled crystals (100 K) at beam lines 14-BM-C (Advanced Photon Source, Argonne) and 7-1 (Stanford Synchrotron Radiation Laboratory, Palo Alto). The cryoprotectant solution consisted of the equilibrated crystallization solution (50 mM MES, pH 5−6, 10−30 mM BOG, 30% saturated ammonium sulfate) with 30% ethylene glycol. Raw diffraction data were processed with DENZO and SCALEPACK (Table 1) (*31*).

Programs CNS (*32*) and XFIT (*33*) were used for structure refinement and model building, respectively. The wild-type $iNOS_{ox}$ crystal structure [PDB code 1NOD, (*21*)], with substrate, H_4B, Trp457, and water molecules omitted, was used as an initial starting model in rigid-body refinement, leading to reduction of R-values from $R = 39.6\%$ ($R_{free} = 38.9\%$) to $R = 29.0\%$ ($R_{free} = 28.4\%$) for W457F, and from $R = 50.1\%$ ($R_{free} = 49.7\%$) to $R = 32.3\%$ ($R_{free} = 32.4\%$) for W457A. The H_4B binding site was rebuilt using $F_o - F_c$ omit electron density maps, while water molecules were modeled based on standard $F_o - F_c$ and $2F_o - F_c$ maps over cycles of minimization and simulated annealing refinement followed by *B*-factor refinement. The final models include residues 77−99, 109−496 for W457F $iNOS_{ox}$, and 77−99, 108−497 for W457A $iNOS_{ox}$. No residues for either mutant structure were found in the disallowed region of the Ramachandran plots obtained using PROCHECK (*34*). LSQKAB from the CCP4 program suite (*35*) was used to obtain superpositions of the crystallographic models and root-mean-square distance deviations among different models.

RESULTS

Overall Structure. We determined crystallographic structures of catalytically active, H_4B-bound W457F (2.6 Å resolution) and W457A (2.3 Å resolution) mutant $iNOS_{ox}$ dimers. The final structural models include all residues of $iNOS_{ox}$ except the terminal residues (amino acids 66−76 and 497−498) and residues surrounding the structural Zn site (amino acids 100−108), where only weak electron density was observed. Difference electron density maps indicate no peaks for the structural Zn ion.[2] High mobility and poor electron density in this region are common in many Zn-free $iNOS_{ox}$ structures (*21, 24*). No peaks were found on an anomalous difference electron density map, further confirming the absence of Zn. The overall structures of both mutants are indistinguishable from the previously reported wild-type $iNOS_{ox}$ structure (*21*). The average root-mean-square distance deviations of Cα positions of 380 residues (residues 116−496) among W457F, W457A, and wild-type $iNOS_{ox}$ subunits are in the range of 0.3 Å. The assembly of mutant $iNOS_{ox}$ subunits into catalytic dimers does not deviate from that seen in wild-type crystallographic structures. Neither mutant structure shows any significant differences at the substrate binding site above the heme when compared to the wild-type. W457A $iNOS_{ox}$ structures with bound *S*-ethylisothiourea determined at lower resolution (unpublished 2.9 and 3.4 Å data) confirm preservation of the wild-type geometry at the heme active site. Thus, the previously reported effects (*26*) of these Trp457 mutations on dimer stability and catalytic activity result from local changes surrounding the H_4B binding site, rather than the propagation of structural changes to the heme active site or dimer assembly.

H_4B Binding Site. In W457F $iNOS_{ox}$, most of the wild-type hydrogen-bonding and *π*-stacking interactions between H_4B and protein residues are preserved (Figure 2A,B and Table 2). H_4B is located between Phe457 of one subunit and Phe470 of an adjacent subunit (Figure 2B). A simulated-annealed omit electron density map indicates the Phe457 side chain is oriented and positioned to form *π*-stacking interactions with H_4B (Figure 2B). As in wild-type Trp457, the backbone carbonyl of Phe457 forms a hydrogen bond with the H_4B N2 (Figure 2B and Table 2). The distance between the centers of the Phe457 ring and the H_4B 2-amino-4-hydroxypyrimidine moiety is 3.8 Å. When the W457F $iNOS_{ox}$ structure is superimposed with the wild-type, the Phe457 side chain overlays with the five-membered moiety of the Trp indole (Figure 2D). An ordered water molecule mediating a hydrogen bond between the Trp457 indole NH and O10 of the H_4B dihydroxypropyl side chain in the wild-type enzyme is not observed in W457F $iNOS_{ox}$. This ordered water molecule, always found in the wild-type NOS_{ox} structures (*21, 23−25*), commonly has a thermal *B*-factor lower than the average overall *B*-factor for a given structure.

The W457A $iNOS_{ox}$ crystal structure shows an unexpected local structural rearrangement that compensates for loss of the bulky aromatic residue at the H_4B binding site. Replace-

[2] The structural Zn ion, which is variably present in recombinant NOS isozymes (*22, 36*), is not required for catalysis (*37*).

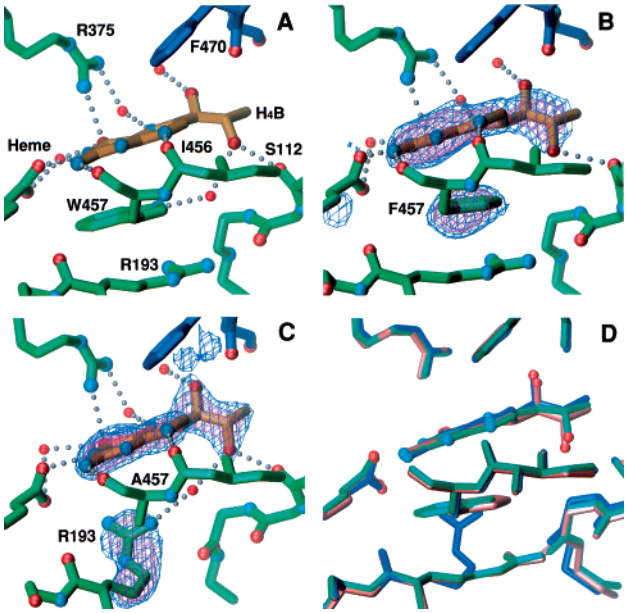

FIGURE 2: H_4B binding site. (A) Hydrogen-bonding (gray dots) and π-stacking interactions between H_4B (orange) and conserved residues and water molecules (red) at the dimer interface in wild-type $iNOS_{ox}$. The bound H_4B interacts with both residues on the same subunit (green) and those provided by the other subunit (blue) of the dimer. (B) A σ_A-weighted $F_o - F_c$ omit map (blue 3.6σ, magenta 5.0σ) showing the bound H_4B and Phe457 side chain in W457F $iNOS_{ox}$. (C) A σ_A-weighted $F_o - F_c$ omit map (blue 3.6σ, magenta 5.0σ) showing the bound H_4B and Arg193 side chain in W457A $iNOS_{ox}$. (D) Superposition of the wild-type (green), W457F (pink), and W457A (blue) H_4B binding sites, showing how the mutations affect the packing of the H_4B site. Water molecules are omitted for clarity.

Table 2: Hydrogen Bond Distances at the H_4B Binding Site for W457 Mutant and Wild-Type $iNOS_{ox}$

structure	W457F	W457A	wild-type (1NOD[a])	wild-type (2NOD)
heme O2A[b]−H_4B N_3 (Å)	2.7	2.8	2.9	2.7
	2.6[c]	2.7	2.8	2.8
heme O2A−H_4B N_2 (Å)	3.2	3.2	3.1	3.1
	2.9	3.2	3.2	3.2
457[d] O−H_4B N_2 (Å)	3.1	2.8	3.0	3.0
	2.9	2.7	2.9	2.9
I456 O−H_4B N_8 (Å)	3.1	3.1	2.9	2.9
	3.1	3.0	3.0	3.1
S112 O−H_4B O10 (Å)	3.2	2.7	2.6	2.8
	3.0	2.6	2.9	2.8
(M114 S−H_4B C_{10})[e] (Å)	5.2	4.6	5.2	5.2
	5.3	4.6	5.2	5.1

[a] PDB codes of wild-type $iNOS_{ox}$ structures with L-Arg (1NOD) and with water molecules (2NOD) at the heme active site (*21*) used for comparison. [b] Nomenclatures correspond to those shown in Figure 1B. [c] Two numbers are obtained from two noncrystallographic symmetry related subunits in the asymmetric unit. [d] Phe457 in W457F, Ala457 in W457A, and Trp457 in wild-type $iNOS_{ox}$. [e] Interatomic distances.

ment of the Trp aromatic ring by Ala at position 457 does not affect the hydrogen bond formed between the Ala457 backbone carbonyl O and H_4B N2 (Table 2); however, it causes the Arg193 side chain to rotate with its guanidinium group oriented almost perpendicularly to the H_4B ring (Figure 2C). An $F_o - F_c$ omit map calculated without the Arg193 side chain shows clear density for the guanidinium group in a T-shaped orientation with the bound cofactor (Figure 2C). The average distance from the terminal nitrogens of Arg193

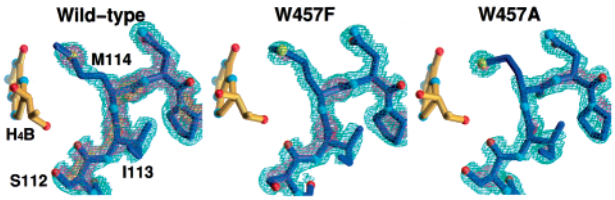

FIGURE 3: N-terminal H_4B binding segment. The bound H_4B (gold) and the 2 $F_o - F_c$ electron density maps (cyan 1σ, magenta 2σ, yellow 3σ) for Ser112−Met114 of the Zn-free wild-type (2.6 Å resolution), W457F (2.6 Å resolution), and W457A (2.3 Å resolution) $iNOS_{ox}$ structures.

to the center of the H_4B 2-amino-4-hydroxypyrimidine is 4.2 Å. This is within the reported range (3.25−4.5 Å) for Arg−aromatic stacking interactions typically found in proteins (*38*). The same movement of Arg193 has been observed in multiple crystal structures of W457A $iNOS_{ox}$, including complexes with *S*-ethylisothiourea or with pterin analogues, H_2B and 4-amino-H_4B (unpublished results). In addition, Arg193 mimics wild-type Trp457 by hydrogen-bonding with a terminal guanidinium nitrogen to the water molecule that interacts with O10 on the H_4B dihydroxypropyl side chain. The average *B*-factor of this water molecule in W457A $iNOS_{ox}$ was 59 Å^2, higher than the average value of 48 Å^2 calculated from all the water molecules in this model.

N-Terminal H_4B Binding Segment. In both the W457F and W457A mutant $iNOS_{ox}$ structures, wild-type interactions of the N-terminal H_4B binding segment (residues Ser112−Met114 in murine iNOS) with H_4B are preserved. The Ser112 carbonyl oxygen hydrogen-bonds to the H_4B dihydroxypropyl side chain, and Met114 packs against the bound cofactor (Figure 3). In W457A mutant $iNOS_{ox}$, however, rearrangement of the Arg193 side chain results in the loss of the wild-type hydrogen bonds to the carbonyl oxygen atoms of Ile113 and Met114. Accordingly, a lower $2F_o - F_c$ electron density is observed in the region of Ser112−Met114, compared to the Zn-free wild-type structure at a comparable resolution (2.6 Å) (Figure 3). However, lower electron density for this region is also observed in the W457F $iNOS_{ox}$ structure (Figure 3), despite conservation of the wild-type hydrogen bonds with Arg193. Therefore, the higher mobility seen in the N-terminal H_4B binding segment does not result simply from the arrangement of Arg193 in the W457A mutant, but rather from the less optimal packing of the H_4B binding site due to the loss of the bulky Trp457 side chain in both W457F and W457A $iNOS_{ox}$.

Hydrogen Bond Network between H_4B and Heme. Effects of the Trp457 mutations on the long-range hydrogen-bonding/stacking network between H_4B and the heme differ between the two Trp457 mutant $iNOS_{ox}$ structures (Figure 4). In W457F $iNOS_{ox}$ (Figure 4B), Phe457 preserves π-stacking interactions with H_4B and maintains the wild-type conformation (Figure 4A) of Arg193, Tyr485, and heme propionate B. The W457A mutation in $iNOS_{ox}$ leads to rearrangement of the Arg193 side chain, reorganizing the hydrogen bond network that connects the H_4B binding site and the heme propionate B (Figure 4C). Although the Tyr485 hydroxyl group remains hydrogen-bonded to the heme propionate B, it no longer hydrogen-bonds to the rearranged Arg193 (Figure 4C). The W457A $iNOS_{ox}$ crystal structure reported here indicates that this mutation leads to changes

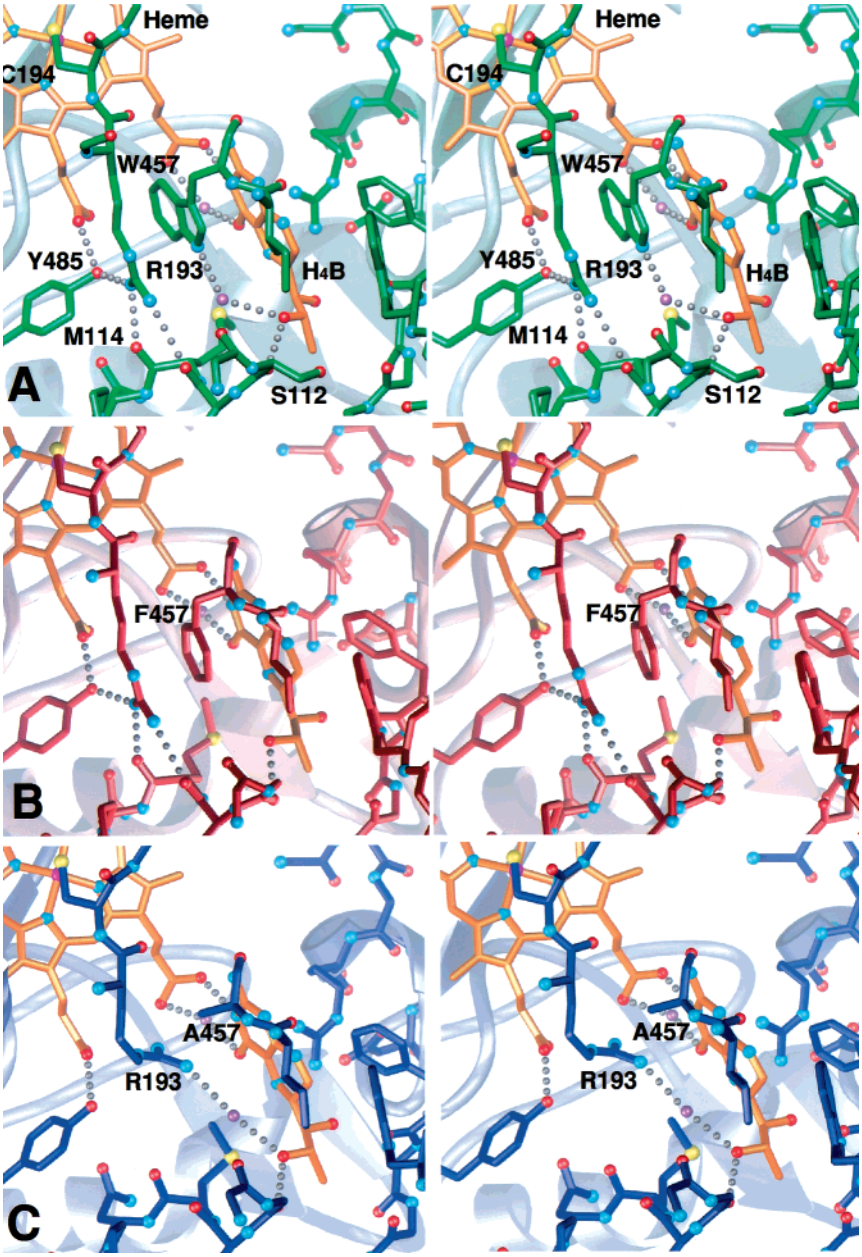

FIGURE 4: Stereoviews of the hydrogen bond network linking the H_4B binding site and the heme site. For clarity, some residues and hydrogen bonds are omitted from the figures. (A) In wild-type $iNOS_{ox}$, Arg193, which stacks with Trp457, forms a hydrogen bond (gray dots) with heme (orange) propionate B via Tyr485. (B) Hydrogen bond configuration surrounding Arg193 and Tyr485 remains unaffected in W457F $iNOS_{ox}$. (C) The W457A mutation causes the Arg193 side chain to rotate, breaking the hydrogen bond with Tyr485.

in long-range interactions among Arg193, Tyr485, and heme propionate B, which appear to be critical for structural integrity of the H_4B binding site.

DISCUSSION

The structural studies of the $iNOS_{ox}$ mutants reported here help distinguish which of the diverse functional roles of H_4B in NOS are modulated by the conserved Trp457. Particularly, we are interested in contributions of this hydrogen-bonded, π-stacking Trp457 to the structural integrity of the H_4B site, H_4B-dependent dimer stability, and electron-transfer processes.

Despite mutations of well-conserved Trp457 at the H_4B binding site, our crystallographic structures show that the wild-type position, orientation, and hydrogen-bonding of H_4B are preserved in both W457F and W457A $iNOS_{ox}$ (Figure 2A−D). Hence, aromaticity at position 457 is not essential for dimer formation, consistent with the earlier mutational studies of $iNOS_{ox}$ (*26*) and full-length nNOS (*27*). Rearrangement of Arg193 in our W457A structure (Figure 2C) provides a structural basis for the differential effects of H_4B on the extent of dimer formation in W457A $iNOS_{ox}$ (*26*) and W678L nNOS (*27*); W457A $iNOS_{ox}$ is 80% dimeric (>90% for wild-type), whereas W678L nNOS is only 15% dimeric (94% for wild-type) in the presence of L-Arg and H_4B. According to our crystallographic structures, the replacement of the bulky Trp side chain with the smallest aliphatic amino acid Ala, not the larger Leu, allows conformational changes of the Arg193 side chain to fill the open space (Figure 2C). The guanidinium group of Arg193 can exert charge-dominant T-shaped stacking effects on bound H_4B, thus achieving stable protein dimerization. The Arg

side chain is known to participate in π-cation interactions with aromatic residues in either T-shaped or parallel geometries (*39*). Similar interactions of Arg with H_4B might explain the unusual naturally occurring NOS from the great pond snail (*40*), which has apparent substitutions of Trp457 with Arg and Arg193 with Gly. The W457A $iNOS_{ox}$ crystal structure reported here reveals the contributions of Arg193 to the H_4B-mediated dimer formation of W457A $iNOS_{ox}$ that were not otherwise apparent.

Both W457F and W457A mutations result in the increased mobility of the N-terminal H_4B binding segment (residues Ser112−Met114 in murine iNOS) (Figure 3), which is located across the dimer interface and may be associated with dimer stability. Substitution of the structural Zn site by a self-symmetric disulfide bond (Cys109 in murine iNOS) at the human $iNOS_{ox}$ dimer interface has been reported to cause a peptide flip at Gly (Gly111 in murine iNOS) and weakening of the hydrogen bond between Ser (Ser112 in murine iNOS) and the H_4B dihydroxypropyl side chain, possibly linking the importance of the structural Zn center and dimer stability (*24*). This flip interpreted at 3 Å resolution, however, was not seen in the equivalent structures of murine $iNOS_{ox}$ dimers at higher resolution (*21, 22*). In the Trp457 mutant $iNOS_{ox}$ structures, the N-terminal H_4B binding region is represented by lower electron density, but the hydrogen bond distances between Ser112 O and H_4B O10 do not change from those in the wild-type enzyme (Table 2), implying that neither the absence of Zn nor the Trp457 mutations significantly propagate to this backbone-mediated interaction at the dimer interface. Although the position of Met114 side chain is affected by the W457A mutation (Table 2), this change is unlikely to influence dimer stability because the M114A $iNOS_{ox}$ mutation does not interfere with dimerization in solution (*41*), and Val occupies this position in bovine and human $eNOS_{ox}$ (*23, 25*). However, in both Trp457 mutants, the loss of the optimal packing provided by the π-stacking Trp457 indole clearly reduces the order of the N-terminal H_4B binding segment. This increased disorder may indicate reduced stability of the H_4B-bound Trp457 mutant $iNOS_{ox}$ dimers, compared to the wild-type enzyme.

The observed conservation of the wild-type structural environment at the heme and substrate binding sites in our Trp457 mutant crystallographic structures is consistent with nearly identical UV−visible heme spectra, heme redox potentials, and O_2 binding data [see the accompanying paper (*28*)]. However, the differences in H_4B-site packing and H_4B-mediated dimer stability might well explain the reported biochemical differences in solution, such as changes in the binding affinity for H_4B and substrate L-Arg (*26*). Likewise, the importance of long-range interactions among H_4B, Trp457, Arg193, and Tyr485 was proposed from the decreased H_4B binding affinity and consequent reduced dimerization of nNOS mutants (*27*), in which the Arg (equivalent to Arg193 in murine iNOS) was mutated to Glu or Leu, and the Tyr (equivalent to Tyr485 in murine iNOS) was mutated to Phe or Leu.

Not only do our Trp457 mutant $iNOS_{ox}$ structures provide insights into the influential roles of Trp457 in structural stability of the H_4B binding site and the $iNOS_{ox}$ dimer, but more importantly in the appropriate tuning of the bound H_4B by the protein for redox activity during NO synthesis. The conservation of key hydrogen-bonding interactions at the H_4B binding site (*22*) among the wild-type, W457F, and W457A $iNOS_{ox}$ structures makes it unlikely that Trp457 mutations alter the oxidation or protonation states of NOS-bound H_4B or disrupt the electron pathway between H_4B and the heme. The Trp457 mutations do not change the positions of the conserved hydrogen-bonding residues at the H_4B binding site (Figure 2 and Table 2), which were previously suggested as crucial in controlling oxidation or protonation states of bound pterins (*22*). Furthermore, these Trp457 mutations do not affect configurations of the direct hydrogen bonds between the heme propionate A, and H_4B N3 and N2 (Figure 2 and Table 2), which were suggested to be key for the electron transfer (*22*). In agreement with our crystal structures, both W457F and W457A mutations have little impact on the extent of pterin radical formation [see the accompanying paper (*28*)]. Therefore, the slower than wild-type rates observed in both W457F and W457A $iNOS_{ox}$ mutants (*28*) for pterin radical formation and coupled heme ferrous−dioxy ($Fe^{II}O_2$) reduction leading to L-Arg hydroxylation (*20*) are not due to disruption of electronic communications between the cofactors or the altered oxidation state of the bound H_4B, but rather due to lack of the optimal stabilizing forces provided by the protein environment to facilitate pterin radical formation.

Relative to wild-type $iNOS_{ox}$, the W457F and W457A mutations are likely to both stabilize the protein binding of the ground-state H_4B and destabilize the protein binding of the H_4B radical. In the wild-type $iNOS_{ox}$ structure, quadrupole moments of the ground-state, protein-bound H_4B and Trp457 indole should produce π-electron clouds with negative electrostatic potential above and below the aromatic rings, favoring pterin radical formation. The decreased π-electron cloud of Phe457 in W457F $iNOS_{ox}$ compared to the wild-type Trp457 should therefore stabilize the protein-bound, ground-state H_4B, and destabilize the protein-bound, neutral or cationic pterin radical, thus slowing radical formation and accelerating its decay, as observed by EPR in the accompanying paper (*28*). In the W457A mutant $iNOS_{ox}$ structure, the rearrangement of positively charged Arg193 to form a T-shaped π-cation interaction with H_4B should further stabilize protein binding to the ground-state H_4B while further destabilizing protein binding to the pterin radical. If H_4B forms a cation radical, as suggested by the $eNOS_{ox}$ crystallographic structure with L-Arg bound at the H_4B site (*23*) and more recently by EPR experiments (*42*), the protein binding of H_4B would be further destabilized by repulsive positive charge distribution between Arg193 and the cofactor. Consistent with these theoretical predictions based on the crystallographic structures, the rate of radical formation is further decreased and the rate of radical decay is further increased in W457A $iNOS_{ox}$, relative to the W457F mutant [see the accompanying paper (*28*)]. In addition, the aforementioned effects of the Trp457 mutations on the mobility at the N-terminal H_4B binding segment and dimer stability may result in dissociation of the pterin radical during catalysis in the full-length enzyme.

In summary, determination and analyses of crystallographic structures of W457F and W457A mutant murine $iNOS_{ox}$ provided insights into the function of hydrogen-bonded, π-stacking Trp457 in the H_4B binding site. Comparisons of the mutant and wild-type structures revealed that the overall fold and dimer assembly of wild-type $iNOS_{ox}$

are preserved in these mutants, as are the conformation and binding modes of both H_4B and heme. The structural biochemistry presented here implicates Trp457 in the integrity of the H_4B binding site, H_4B-mediated dimer stability, and the regulation of electron transfer during NO synthesis. Although Trp457 is not required for dimer formation, the aromaticity at position 457 is important for the spatial packing that integrates the heme and H_4B binding sites, and for the stability of H_4B-bound dimers. Our crystallographic analyses together with spectroscopic and kinetic analyses [see the accompanying paper (*28*)] provide insights into how the π-stacking Trp457 maintains the optimal stabilizing environment for regulating the rate of electron transfer between H_4B and the heme $Fe^{II}O_2$ intermediate, a step required for L-Arg hydroxylation in NOS catalysis.

ACKNOWLEDGMENT

We thank the Advanced Photon Source (APS) and the Stanford Synchrotron Radiation Laboratory (SSRL) for use of data collection facilities, AstraZeneca for AR-C95791AA, R. J. Rosenfeld, E. D. Garcin, C. D. Putnam, C. D. Mol, and S. S. Parikh for assistance with data analyses, structure refinement, and helpful discussions, and F. Himo and L. Noodleman for discussions on π-stacking and π-cation interactions.

REFERENCES

1. Griffith, O. W., and Stuehr, D. J. (1995) *Annu. Rev. Physiol. 57*, 707−736.
2. Marletta, M. A. (1993) *J. Biol. Chem. 268*, 12231−12234.
3. Stuehr, D. J. (1999) *Biochim. Biophys. Acta 1411*, 217−230.
4. Bredt, D. S., and Snyder, S. H. (1990) *Proc. Natl. Acad. Sci. U.S.A. 87*, 682−685.
5. Marsden, P. A., Schappert, K. T., Chen, H. S., Flowers, M., Sundell, C. L., Wilcox, J. N., Lamas, S., and Michel, T. (1992) *FEBS Lett. 307*, 287−293.
6. Hemmens, B., and Mayer, B. (1998) *Methods Mol. Biol. 100*, 1−32.
7. Siddhanta, U., Presta, A., Fan, B., Wolan, D., Rousseau, D. L., and Stuehr, D. J. (1998) *J. Biol. Chem. 273*, 18950−18958.
8. Panda, K., Ghosh, S., and Stuehr, D. J. (2001) *J. Biol. Chem. 276*, 23349−23356.
9. Abu-Soud, H. M., Loftus, M., and Stuehr, D. J. (1995) *Biochemistry 34*, 11167−11175.
10. Tzeng, E., Billiar, T. R., Robbins, P. D., Loftus, M., and Stuehr, D. J. (1995) *Proc. Natl. Acad. Sci. U.S.A. 92*, 11771−11775.
11. Baek, K. J., Thiel, B. A., Lucas, S., and Stuehr, D. J. (1993) *J. Biol. Chem. 268*, 21120−21129.
12. Stuehr, D. J., Cho, H. J., Kwon, N. S., Weise, M. F., and Nathan, C. F. (1991) *Proc. Natl. Acad. Sci. U.S.A. 88*, 7773−7777.
13. Albakri, Q. A., and Stuehr, D. J. (1996) *J. Biol. Chem. 271*, 5414−5421.
14. Cho, H. J., Martin, E., Xie, Q. W., Sassa, S., and Nathan, C. (1995) *Proc. Natl. Acad. Sci. U.S.A. 92*, 11514−11518.
15. Ghosh, D. K., Wu, C., Pitters, E., Moloney, M., Werner, E. R., Mayer, B., and Stuehr, D. J. (1997) *Biochemistry 36*, 10609−10619.
16. Mayer, B., Wu, C., Gorren, A. C., Pfeiffer, S., Schmidt, K., Clark, P., Stuehr, D. J., and Werner, E. R. (1997) *Biochemistry 36*, 8422−8427.
17. Presta, A., Siddhanta, U., Wu, C., Sennequier, N., Huang, L., Abu-Soud, H. M., Erzurum, S., and Stuehr, D. J. (1998) *Biochemistry 37*, 298−310.
18. Bec, N., Gorren, A. C., Voelker, C., Mayer, B., and Lange, R. (1998) *J. Biol. Chem. 273*, 13502−13508.
19. Hurshman, A. R., Krebs, C., Edmondson, D. E., Huynh, B. H., and Marletta, M. A. (1999) *Biochemistry 38*, 15689−15696.
20. Wei, C. C., Wang, Z. Q., Wang, Q., Meade, A. L., Hemann, C., Hille, R., and Stuehr, D. J. (2001) *J. Biol. Chem. 276*, 315−319.
21. Crane, B. R., Arvai, A. S., Ghosh, D. K., Wu, C., Getzoff, E. D., Stuehr, D. J., and Tainer, J. A. (1998) *Science 279*, 2121−2126.
22. Crane, B. R., Arvai, A. S., Ghosh, S., Getzoff, E. D., Stuehr, D. J., and Tainer, J. A. (2000) *Biochemistry 39*, 4608−4621.
23. Raman, C. S., Li, H., Martásek, P., Kral, V., Masters, B. S. S., and Poulos, T. L. (1998) *Cell 95*, 939−950.
24. Li, H., Raman, C. S., Glaser, C. B., Blasko, E., Young, T. A., Parkinson, J. F., Whitlow, M., and Poulos, T. L. (1999) *J. Biol. Chem. 274*, 21276−21284.
25. Fischmann, T. O., Hruza, A., Niu, X. D., Fossetta, J. D., Lunn, C. A., Dolphin, E., Prongay, A. J., Reichert, P., Lundell, D. J., Narula, S. K., and Weber, P. C. (1999) *Nat. Struct. Biol. 6*, 233−242.
26. Ghosh, S., Wolan, D., Adak, S., Crane, B. R., Kwon, N. S., Tainer, J. A., Getzoff, E. D., and Stuehr, D. J. (1999) *J. Biol. Chem. 274*, 24100−24112.
27. Sagami, I., Sato, Y., Daff, S., and Shimizu, T. (2000) *J. Biol. Chem. 275*, 26150−26157.
28. Wang, Z.-Q., Wei, C.-C., Ghosh, S., Meade, A., Hemann, C., Hille, R., and Stuehr, D. J. (2001) *Biochemistry* (in press).
29. Gachhui, R., Ghosh, D. K., Wu, C., Parkinson, J., Crane, B. R., and Stuehr, D. J. (1997) *Biochemistry 36*, 5097−5103.
30. Crane, B. R., Rosenfeld, R. J., Arvai, A. S., Ghosh, D. K., Ghosh, S., Tainer, J. A., Stuehr, D. J., and Getzoff, E. D. (1999) *EMBO J. 18*, 6271−6281.
31. Otwinowski, Z., and Minor, W. (1997) *Methods Enzymol. 276*, 307−326.
32. Brünger, A. T., Adams, P. D., Clore, G. M., DeLano, W. L., Gros, P., Grosse-Kunstleve, R. W., Jiang, J. S., Kuszewski, J., Nilges, M., Pannu, N. S., Read, R. J., Rice, L. M., Simonson, T., and Warren, G. L. (1998) *Acta Crystallogr., Sect. D D54*, 905−921.
33. McRee, D. E. (1999) *J. Struct. Biol. 125*, 156−165.
34. Laskowski, R. A., MacArthur, M. W., Moss, D. S., and Thornton, J. M. (1993) *J. Appl. Crystallogr. 26*, 283−291.
35. Collaborative Computational Project, Number 4 (1994) *Acta Crystallogr., Sect. D D50*, 760−763.
36. Miller, R. T., Martásek, P., Raman, C. S., and Masters, B. S. S. (1999) *J. Biol. Chem. 274*, 14537−14540.
37. Hemmens, B., Goessler, W., Schmidt, K., and Mayer, B. (2000) *J. Biol. Chem. 275*, 35786−35791.
38. Flocco, M. M., and Mowbray, S. L. (1994) *J. Mol. Biol. 235*, 709−717.
39. Gallivan, J. P., and Dougherty, D. A. (1999) *Proc. Natl. Acad. Sci. U.S.A. 96*, 9459−9464.
40. Korneev, S. A., Piper, M. R., Picot, J., Phillips, R., Korneeva, E. I., and O'Shea, M. (1998) *J. Neurobiol. 35*, 65−76.
41. Ghosh, D. K., Crane, B. R., Ghosh, S., Wolan, D., Gachhui, R., Crooks, C., Presta, A., Tainer, J. A., Getzoff, E. D., and Stuehr, D. J. (1999) *EMBO J. 18*, 6260−6270.
42. Schmidt, P. P., Lange, R., Gorren, A. C. F., Werner, E. R., Mayer, B., and Andersson, K. K. (2001) *J. Biol. Inorg. Chem. 6*, 151−158.

BI011183K